

Fourier transform spectroscopy and coupled-channel deperturbation treatment of the $A^1\Sigma^+ \sim b^3\Pi$ complex of KCs molecule

A. Kruzins, I. Klincare, O. Nikolayeva, M. Tamanis, R. Ferber
Laser center, University of Latvia, Rainis Boulevard 19, LV-1586 Riga, Latvia

E. A. Pazyuk, A. V. Stolyarov
*Department of Chemistry, Moscow State University,
 GSP-2 Leninskie gory 1/3, Moscow 119992, Russia*

(Dated: November 10, 2018)

The laser induced fluorescence (LIF) spectra $A^1\Sigma^+ \sim b^3\Pi(E^J) \rightarrow X^1\Sigma^+$ of KCs dimer were recorded in near infrared region by Fourier Transform Spectrometer with a resolution of 0.03 cm^{-1} . Overall more than 200 collisionally enhanced LIF spectra were rotationally assigned to $^{39}\text{K}^{133}\text{Cs}$ and $^{41}\text{K}^{133}\text{Cs}$ isotopomers yielding with the uncertainty of $0.003\text{-}0.01 \text{ cm}^{-1}$ more than 3400 rovibronic term values of the strongly mixed singlet $A^1\Sigma^+$ and triplet $b^3\Pi$ states. Experimental data massive starts from the lowest vibrational level $v_A = 0$ of the singlet and nonuniformly cover the energy range $E^J \in [10040, 13250] \text{ cm}^{-1}$ with rotational quantum numbers $J \in [7, 225]$. Besides of the dominating regular $A^1\Sigma^+ \sim b^3\Pi_{\Omega=0}$ interactions the weak and local heterogenous $A^1\Sigma^+ \sim b^3\Pi_{\Omega=1}$ perturbations have been discovered and analyzed. Coupled-channel deperturbation analysis of the experimental $^{39}\text{K}^{133}\text{Cs}$ e -parity termvalues of the $A^1\Sigma^+ \sim b^3\Pi_{\Omega=0,1,2}$ complex was accomplished in the framework of the phenomenological 4×4 Hamiltonian accounting implicitly for regular interactions with the remote $^1\Pi$ and $^3\Sigma^+$ states manifold. The resulting diabatic potential energy curves of the interacting states and relevant spin-orbit coupling matrix elements defined analytically by Expanded Morse Oscillators model reproduce 95% of experimental data field of the $^{39}\text{K}^{133}\text{Cs}$ isotopomer with a standard deviation of 0.004 cm^{-1} which is consistent with the uncertainty of the experiment. Reliability of the derived parameters was additionally confirmed by a good agreement between the predicted and experimental termvalues of $^{41}\text{K}^{133}\text{Cs}$ isotopomer. Calculated relative intensity distributions in the $A \sim b \rightarrow X$ LIF progressions are also consistent with their experimental counterparts. Finally, the deperturbation model was applied for a simulation of pump-dump optical cycle $a^3\Sigma^+ \rightarrow A^1\Sigma^+ \sim b^3\Pi \rightarrow X^1\Sigma^+$ proposed for transformation of ultracold colliding K+Cs pairs to their ground molecular state $v_X = 0; J_X = 0$.

PACS numbers:

I. INTRODUCTION

In ultracold (below 1 mK) gases of polar alkali diatomic molecules the electric dipole-dipole interaction possesses long-range and anisotropic character and cause particular attraction since they are promising for a variety of novel applications [1]. Among them there are proposals of quantum phase transitions [2], quantum information devices [3], coherent control of chemical reactions [4]. Further success in producing ensembles of ultracold quantum gases of diatomic molecules relies on the accurate knowledge of the molecular rovibronic structure and transition probabilities gained from the high resolution spectroscopy and state of art *ab initio* calculations.

As far as polar alkali diatomic molecules are considered, experiment based information on the potential energy curves of the lowest excited $A^1\Sigma^+$ and $b^3\Pi$ states mixed by singlet-triplet spin-orbit (SO) interaction is of great importance due to the

possibility of their usage as intermediate states for transferring the vibrationally excited molecules obtained from cold colliding atoms via photoassociation or Feshbach resonances into the absolute rovibronic ground states $X^1\Sigma^+$ with $v_X = 0, J_X = 0$ [5, 6]. In the sequence of heteronuclear alkali diatomics KCs is among promising species for producing ultracold polar quantum gases. Due to proximity of K($4p$) and Rb($5p$) energies, the energy of low-lying electronic states of KCs is similar to the ones in the RbCs molecule, however, KCs possess larger permanent electric dipole moment. The RbCs molecule has been already studied in ultracold conditions [7, 8, 9]. In particular, the recent quantum dynamics simulation of the mixed $A^1\Sigma^+$ and $b^3\Pi_{\Omega}$ states of RbCs in a time-dependent wave-packet approach [6] demonstrated that the pump - dump picosecond pulsed laser scheme could be efficient to form ultracold heteronuclear diatomic molecules in highly bonded ground $X^1\Sigma^+$ state. The highly accurate em-

pirical potentials for the ground singlet $A^1\Sigma^+$ and triplet $a^3\Sigma^+$ states converging to the lowest $K(4S)+Cs(6S)$ asymptote (see Fig. 1) as well as predicted scattering lengths and Feshbach resonances which are required to simulate cold collision processes are presented in Ref's [10, 11]. However, till now there is no empirical information about the excited states of KCs while *ab initio* potential energy curves (PECs) have been calculated for a wide range of internuclear distance in the framework of pure Hund's (a) [12, 13, 14] and (c) [15] coupling cases. The relevant permanent and transition dipole moment functions are also available from Ref's [13, 14].

Particular complicated objects for the theoretical interpretation are alkali diatomics containing a heavy Rb or Cs atoms since the relevant singlet-triplet SO coupling matrix element $\xi_{Ab_0}^{so}$ between $A^1\Sigma^+$ and $b^3\Pi_{\Omega=0}$ states is comparable with vibrational spacing of the interacting states. Therefore $A^1\Sigma^+$ and $b^3\Pi_{\Omega=0}$ states are fully mixed (later denoted as the $A \sim b$ complex) in both adiabatic and diabatic basis set representation [16]. First studies of such kind of system have been reported for the Rb-containing alkali diatomics, in which apparent disorder in vibrational spacing was observed for Rb_2 [17], see [18] for more extensive studies, $NaRb$ [19] and $RbCs$ [20]. The crucial issue however remained unsolved, namely, while the experimental term values were obtained with high precision of about $0.003-0.01 \text{ cm}^{-1}$, the resulting deperturbed parameters reproduced experimental data with much poorer accuracy of $0.05-0.25 \text{ cm}^{-1}$ [18, 19, 20]. Furthermore, even the vibrational numbering of the "dark" triplet $b^3\Pi$ state was still remained questionable.

In recent studies on the $A \sim b$ complex of $NaRb$ [21] and $NaCs$ [22] more comprehensive deperturbation method has been developed in the framework of the inverted channel-coupling approach by means of the 4×4 Hamiltonian for the $A^1\Sigma^+$ and $b^3\Pi_{\Omega=0,1,2}$ substates constructed on Hund's coupling case (a) basis functions. Phenomenological inclusion of the splitting of the $b^3\Pi_{\Omega=0,1,2}$ substates and of indirect $A^1\Sigma^+$ and $b^3\Pi_{\Omega=1}$ states coupling allowed accounting for the regular perturbation. The elaborated model reproduced the experimental term values obtained by the high resolution Fourier transform spectroscopy (FTS) of the laser induced fluorescence (LIF) from/to the $A \sim b$ complex with a standard deviation of $0.006-0.012 \text{ cm}^{-1}$, which was consistent with the uncertainty of the FTS experiment. The paper [22] presents the most challenging though attractive,

both for model's testing and applications, case of $A \sim b$ complex study of a Cs-atom containing alkali diatomics where SO interaction is of largest value mainly determined by $\xi_{so} \sim 185 \text{ cm}^{-1}$ for $6^2P(Cs)$. This successful approach opens the path to study of the $A \sim b$ complex of more heavier Cs-containing heteronuclear alkali diatomic such as $RbCs$ and KCs . While the $RbCs$ molecule is currently under investigation [23] the present paper deals with the KCs molecule.

It should be noted that the present experimental and deperturbation studies of the KCs $A \sim b$ complex are greatly facilitated by the couple of facts. First, the KCs molecule was recently involved in detailed FTS LIF investigation [10] which resulted in high accuracy empirical point-wise PEC for the ground $X^1\Sigma^+$ state covering a range $v_X = 0$ to 97 and $J_X = 12$ to 209. Moreover, a majority of the data for PEC construction in [10] was obtained directly from the $(A \sim b) \rightarrow X$ LIF spectra containing the information on rovibronic energies of the $A \sim b$ complex. Second, the accurate *ab initio* spin-orbit coupling matrix elements between the lowest electronic states of KCs have been obtained recently in Ref. [14] as explicit functions of internuclear distance.

The goal of the present work is to perform high-resolution spectroscopy studies of the $A \sim b$ complex of the KCs molecule and to apply the adequate data processing in order to get empirical molecular structure parameters, namely the deperturbed $A^1\Sigma^+$ and $b^3\Pi$ diabatic potential energy curves along with the related SO coupling matrix elements functions on internuclear distance R .

In summary, Sections II and III present the experimental techniques and spectra analysis, Section IV presents the deperturbation model and computational details, Section V includes obtained fitted parameters, as well as interpretation of experimental data. The paper ends with short conclusion (Section VI).

II. EXPERIMENT

In the experiment the rovibronic levels of the KCs $A \sim b$ complex were directly excited by diode lasers and subsequent $(A \sim b) \rightarrow X$ LIF spectra were recorded by Fourier transform spectrometer. The experimental setup was the same as used for KCs ground state studies [10] and, hence, we will mention here only some key points of the experiment. KCs molecules were produced in a linear stainless steel heat pipe. The heat pipe was filled

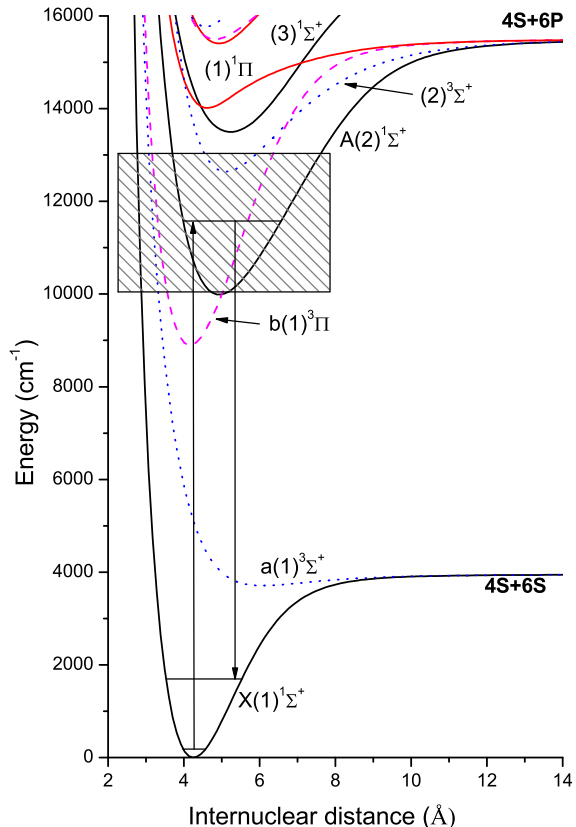


FIG. 1: (Color online) Scheme of electronic terms based on *ab initio* results of Ref. [12]

with 10 g of K (natural isotope mixture) and 7 g of Cs (both metals in ampules from Alfa Aesar). The typical operating pressure of Ar buffer gas in the heat pipe was 3-5 mbar. On the one hand Ar gas prevented condensation of the metal vapor on the heat pipe windows, and, on the other hand, collisions of optically excited KCs molecules in particular rovibronic levels v' , J' with Ar atoms ensured population of great number of neighboring rotational levels and observation of the respective transitions to the ground state. During the experiments the heat pipe was kept at 270 – 290°C temperature by a Carbolite furnace.

In the experiment the laser beam was sent into the heat pipe through a pierced mirror. Backward LIF was collected by the same mirror and focused, by two lenses, on the input aperture of the spectrometer (Bruker IFS 125HR). For LIF detection we used an InGaAs diode operated at room temperature. The spectral sensitivity of the detec-

tor gradually diminishes from about 6500 cm^{-1} toward higher frequencies reaching 60% of maximal sensitivity at $\sim 10000 \text{ cm}^{-1}$. Then sensitivity drops much faster, reaching 10-15% of maximal value at 11000 cm^{-1} . The resolution of the spectrometer was typically set to 0.03 cm^{-1} .

The ($A \sim b$) $\leftarrow X$ transitions were excited by tunable diode lasers. Four single mode laser diodes with central wavelengths 850 nm (LD850/100 from Toptica Photonics), 980 nm (L980P200I from Thorlabs), 1020 nm (LD-1020-0400 from Toptica Photonics) and 1060 nm (L1060P100J from Thorlabs) were mounted in homemade external cavity resonators (Littrow configuration) with a grating serving as a feedback source. The respective frequency tuning ranges were 11560 - 11930 cm^{-1} , 10209 - 10515 cm^{-1} , 9700-9860 cm^{-1} , and 9360-9510 cm^{-1} . Fine tuning of the grating was achieved by a piezoelectric actuator. Temperature and current stabilization was ensured by Thorlabs controllers. The power of the lasers at the entrance of the heat pipe varied from 15 to about 50 mW depending on particular laser diode and laser current. The general approach to measurements was the following. The laser frequency was tuned until the LIF signal monitored at reduced resolution in the “Preview Mode” of the spectrometer gets its maximal value and then fixed during recording of the spectrum. In order to ensure sufficient signal-to-noise ratio for the lines of medium strength, the number of scans for each recorded spectrum varied from 20 to 40; averaging over a number of repeated measurements was applied in some cases. In some cases the strong scattered laser light from the input window of the heat pipe was eliminated by long-pass edge filters.

III. ANALYSIS OF THE SPECTRA

Recorded KCs LIF spectra, see Figs. 2-5, typically consisted of one or two strong doublet progressions and several weaker ones.

The assignment of the LIF progressions in the ($A \sim b$) $\rightarrow X$ spectra was straightforward from measured vibrational and rotational spacings thanks to accurate ground state PEC [10]. The term values of the upper rovibronic levels of the $A \sim b$ complex giving rise to ($A \sim b$) $\rightarrow X$ LIF were obtained by adding the corresponding ground state level energy to a transition wave number. The uncertainty of the line positions is estimated to be 0.1 of the resolution, or 0.003 cm^{-1} . For lines with signal-to-noise ratio (SNR) less than 3

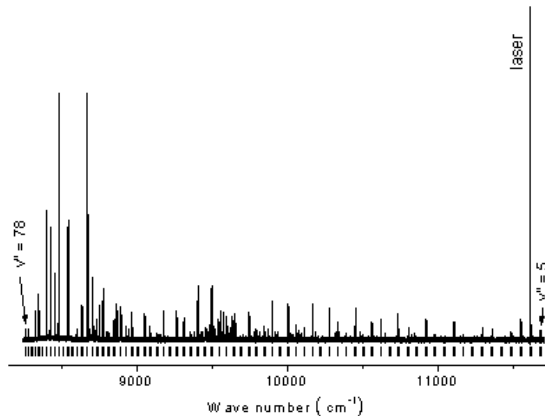


FIG. 2: $^{39}\text{K}^{133}\text{Cs}$ ($A \sim b$) \rightarrow X LIF spectrum recorded by InGaAs detector at excitation with 850nm laser diode (laser frequency 11608.623 cm^{-1}). The strongest doublet P_{63}, R_{61} progression $5 \leq v_X \leq 78$ originates from the level $J' = 62$ with energy $E' = 12164.984\text{ cm}^{-1}$ excited by the transition $(v^*, 62) \leftarrow (6, 63)$. Another weaker KCs LIF progression excited in $(v^*, 133) \leftarrow (6, 134)$ transition is not marked. A mesh of weaker lines around 9500 cm^{-1} belongs to K_2 LIF.

the uncertainty increases and was assumed to be about 0.01 cm^{-1} for lines with SNR of about 2. The term values of the upper state levels were determined as average value from at least four transitions. Hence, the main uncertainty of the term values could be caused by the shift (if any) of the laser frequency from the center of the Doppler broadened ($A \sim b$) \leftarrow X absorption line. When LIF is registered, as in our case, along the direction of the laser beam, this shift is transferred to the respective shift of the LIF line positions. The Doppler broadening for KCs at the exploited spectral region is about 0.012 cm^{-1} and we estimate maximal experimental uncertainty of the $A \sim b$ complex term values as 0.01 cm^{-1} .

Typically, around the strong LIF lines the satellite lines could be recorded due to collision - induced distribution of the population of the directly excited rovibronic level over neighboring rotational levels and even vibrational levels. The assignment of these lines was based on the high accuracy of the ground state PEC and it was always checked that the spacing of satellite doublet lines ($v_R - v_P$) coincides with calculated energy differences between

the respective ground state rotational levels within accuracy of some milliwavenumbers.

Figure 2 represents an example of the recorded LIF spectrum when the ($A \sim b$) \leftarrow X transition is excited with the 850 nm laser diode tuned to 11608.623 cm^{-1} . The recorded spectral line intensities for frequencies above 10000 cm^{-1} are substantially diminished because of dropping of the spectral sensitivity of the InGaAs detector. The LIF intensity distribution in such a long progression as depicted in Fig. 2, with strong last maximum at high v_X , is characteristic for highly excited vibrational levels v_A of the $A \sim b$ complex. Note that, in general, the LIF spectra recorded with 850 nm diode excitation usually contained a very strong $A^1\Sigma_u \rightarrow X^1\Sigma_g$ band of K_2 , and only by careful selection of the laser frequencies it was possible to eliminate the K_2 fluorescence, at the same time having strong enough KCs ($A \sim b$) \rightarrow X LIF progressions.

The usage of 1020 nm and 1050 nm laser diodes allowed us to reach low lying A - state rovibronic levels of KCs. Rather strong LIF signal made it possible in a number of cases to detect spectra without filtering of scattered laser light. Thus, full LIF progressions could be recorded, which was important for establishing the relative intensity distribution in the progressions, which is helpful for vibrational assignment of the upper state. The example of such a spectrum is given in Fig. 3. This spectrum contains five assigned KCs ($A \sim b$) \rightarrow X progressions, two of them with $J' = 50$ and 109 are originating from the lowest v_A level with predominant singlet character. These two progressions show unusual intensity distribution. Along with one strong bell - shape maximum in intensity distribution around 9500 cm^{-1} at low v_X , as is typical for progressions from upper state $v' = 0$ vibrational level, we have found for these progressions transitions to higher v_X resulting in additional intensity maximum, however substantially weaker than the main one. The small fragment of the spectrum with these additional transitions is given in Fig. 3b. Besides, the spectrum in Fig. 3 contains a progression originating from the level with energy $E' = 10227.038\text{ cm}^{-1}$ and $J' = 44$ which is of predominantly triplet character as will be shown below, see Section V. A short fragment of this progression can be seen in Fig. 3b where the respective P, R -doublets are marked above the spectrum. In general, the laser most often excited the levels with a dominant singlet character, and only in some cases a direct excitation of rovibronic ($A \sim b$)-state levels with a dominant triplet char-

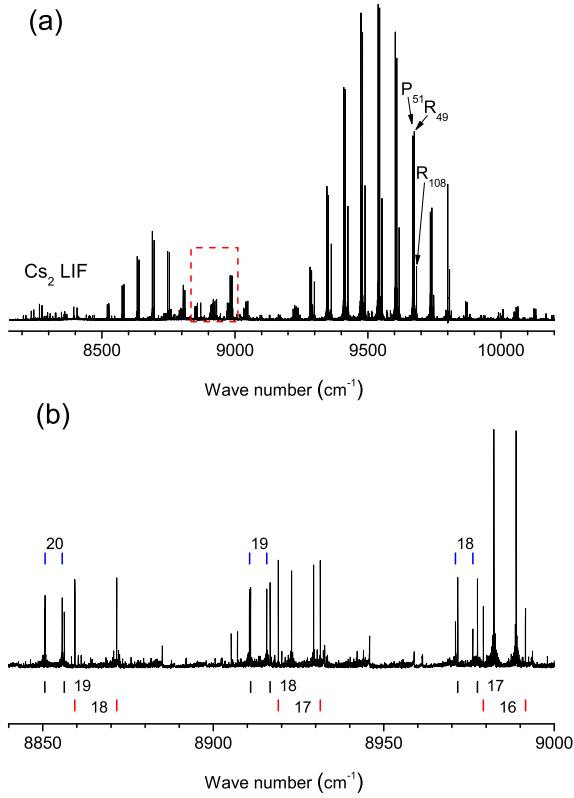


FIG. 3: (a) The $^{39}\text{K}^{133}\text{Cs}$ ($A \sim b$) \rightarrow X LIF spectrum recorded at laser frequency 9800.135 cm^{-1} . The following ($A \sim b$) \leftarrow X ; (v^*, J') \leftarrow (v_X, J_X) excitation transitions have been assigned: ($v^*, 50$) \leftarrow ($4, 51$); ($v^*, 109$) \leftarrow ($3, 110$); ($v^*, 57$) \leftarrow ($7, 56$); ($v^*, 123$) \leftarrow ($16, 122$); ($v^*, 44$) \leftarrow ($5, 43$). Weak Cs_2 progressions have been assigned below 8500 cm^{-1} . An indexes for P_{J_X}, R_{J_X} lines denote the respective ground state rotational levels. (b) The zoomed fragment of the spectrum; doublets originating from the lowest excited vibrational level possessing dominant singlet character with $J' = 50$ and $J' = 109$ are marked with black and red vertical bars below the spectrum. The bars above the spectrum mark transitions from the level ($v^*, J' = 44$) with dominant triplet character. Numbers at bars denote v_X .

acter took place.

Fig. 4 and Fig. 5 demonstrate how fruitful is the collision induced rotational relaxation for systematic study of the $A \sim b$ complex level structure. The spectrum in Fig. 4a contains one very strong progression originating from the level $E' = 10255.413 \text{ cm}^{-1}$, $J' = 49$ as well as five weaker ones. A large number of satellite lines was as-

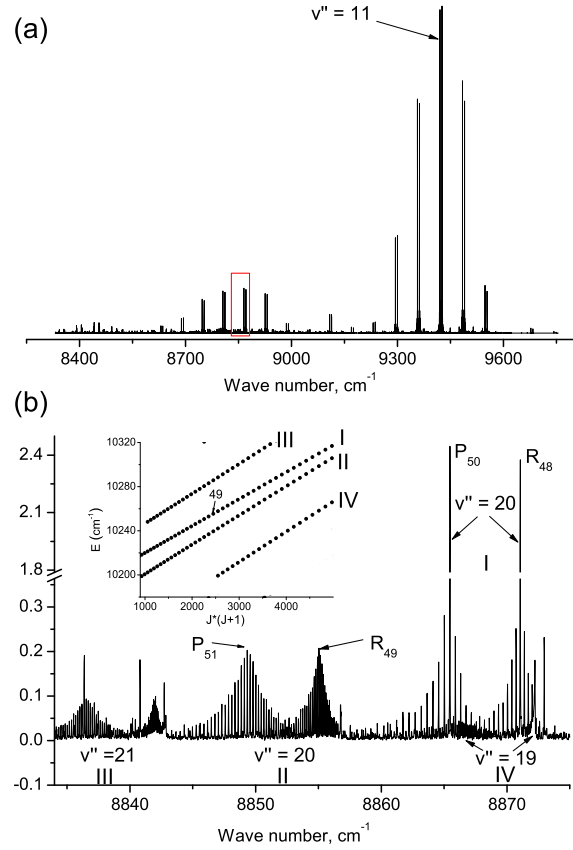


FIG. 4: (a) The $^{39}\text{K}^{133}\text{Cs}$ ($A \sim b$) \rightarrow X LIF spectrum recorded at excitation frequency 9743.083 cm^{-1} . The scattered laser light and LIF at frequencies higher than about 9500 cm^{-1} are cut by a long-pass edge filter. The following excitation transitions for $^{39}\text{K}^{133}\text{Cs}$ have been assigned: ($v^*, 49$) \leftarrow ($6, 50$); ($v^*, 81$) \leftarrow ($17, 82$); ($v^*, 25$) \leftarrow ($13, 26$); ($v^*, 135$) \leftarrow ($12, 134$); ($v^*, 150$) \leftarrow ($11, 149$). (b) Zoomed part of the spectrum around $v_X = 20$ for the strongest progression with $J' = 49$. Three groups (II-IV) of satellite P, R branches shifted from the main rotational relaxation pattern (group I) are clearly seen. The inset presents term values of the respective rovibronic levels as dependent of $J(J+1)$. Directly excited level $J' = 49$ is marked.

signed around the strong P_{50}, R_{48} doublet lines, especially at transitions to $v_X = 11$. The most interesting feature consists in appearance of the additional three wide groups of P, R satellite lines, as seen in Fig. 4b. These groups are shifted from the main P_{50}, R_{48} doublet and represent a situation when an initial population of the optically excited

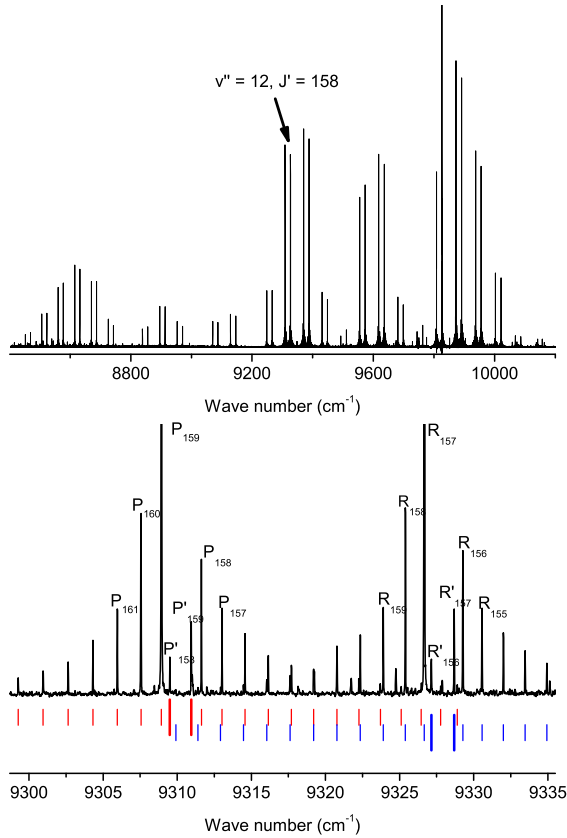


FIG. 5: (Color online) (a) The LIF spectrum recorded at excitation frequency 9826.348 cm^{-1} . The strongest progression originates from the upper level excited in transition $(v'', 158) \leftarrow (4, 157)$. (b) zoomed part of the spectrum around $v_X = 12$; Red and blue bars denote assigned P and R satellite lines respectively. Long bars mark transitions from upper state levels with dominant triplet $b^3\Pi_1$ character. Numbers in the spectrum denote corresponding ground state rotational quantum numbers for observed transitions.

level with $J' = 49$ is collisionally distributed within two state ($A^1\Sigma^+$ and $b^3\Pi_0$) rovibronic level manifolds of the $A \sim b$ complex. As a result, more than 130 term values were obtained from this spectrum, see the inset in Fig. 4b. Note that these satellite groups are the strongest in the range $8700 \text{ cm}^{-1} - 9000 \text{ cm}^{-1}$ and substantially weaker at higher frequency (lower v_X) range.

In several spectra clear evidences of local perturbations were observed as illustrated in Fig. 5. The spectrum given in Fig. 5a is recorded at excitation frequency 9826.348 cm^{-1} ; it consists of

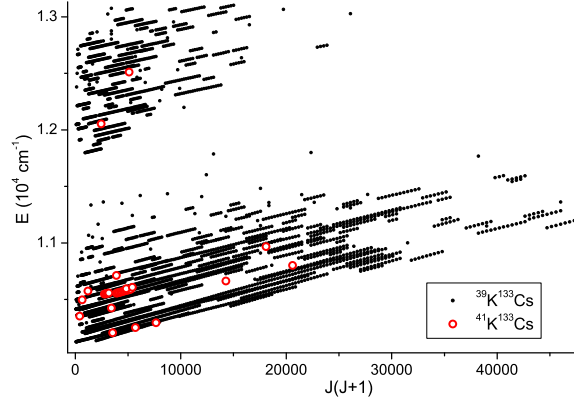


FIG. 6: (Color online) Experimental term values of the ($A^1\Sigma^+ \sim b^3\Pi$) complex plotted versus $J'(J' + 1)$.

one strong KCs LIF progression from the level ($E' = 10861.046 \text{ cm}^{-1}$, $J' = 158$) and several weak KCs and K_2 LIF progressions, hardly seen in this scale. Zoomed part of the strong progression in the range of $v_X = 12$ is given in Fig. 5b. Along with an ordinary satellite line pattern around the central P, R lines with gradually changing spacing between the lines, the local perturbation can be clearly recognized from the two gaps (“windows”) in the both P, R branches, see P_{159}/P_{158} and R_{157}/R_{156} . Moreover, we have assigned “extra” lines with the same rotational quantum numbers, namely P'_{158} , P'_{159} , R'_{156} and R'_{157} , see Fig. 5b. As it will be shown later these additional lines take their origin from the levels with dominant $b^3\Pi_1$ state character and they can be seen here due to effective collisional transfer of population from the directly excited predominantly singlet A state level with $J' = 158$, since it is very close to the perturbation center.

Overall such local perturbations accompanied with extra lines were observed in three spectra. In several cases the local perturbations were observed as irregularities in line sequences without “extra” lines.

Summarizing, during this study more than 3400 term values of the $A \sim b$ complex rovibronic levels were obtained. These term values are given in Fig. 6 as dependent on $J'(J' + 1)$. Empty circles seen in Fig. 6 show distribution of 31 term value determined for the $^{41}\text{K}^{133}\text{Cs}$ levels. The data for $^{41}\text{K}^{133}\text{Cs}$ are given also in Table I.

TABLE I: The experimental rovibronic termvalues E^{expt} (in cm^{-1}) of the of $^{41}\text{K}^{133}\text{Cs}$ isotopomer assigned to the $A^1\Sigma^+ \sim b^3\Pi$ complex. $\Delta = E^{expt} - E^{CC}$ is the difference between experimental and predicted energies. P_i (in %) are fractional partition of the levels, see Section V.

J'	E^{expt}	Δ	P_A	P_{b0}	P_{b1}
59	10205.767	0.003	44.9	55.1	0.0
75	10250.792	-0.001	85.2	12.7	2.1
58	10424.388	0.001	65.8	34.2	0.0
52	10547.339	-0.008	66.3	33.5	0.2
53	10549.850	-0.008	66.8	32.9	0.3
54	10552.405	-0.007	67.2	32.3	0.5
55	10555.010	0.000	67.5	31.6	0.9
56	10557.639	-0.014	67.5	30.7	1.8
62	10555.967	-0.003	51.1	48.8	0.1
63	10559.120	0.001	50.4	49.5	0.1
64	10562.317	-0.007	49.7	50.2	0.1
65	10565.579	-0.007	49.0	50.9	0.1
66	10568.900	-0.006	48.3	51.6	0.1
67	10572.278	-0.005	47.6	52.4	0.1
68	10575.711	-0.006	46.8	53.1	0.1
69	10579.199	-0.010	46.1	53.8	0.1
70	10582.754	-0.007	45.3	54.6	0.1
71	10586.355	-0.014	44.6	55.3	0.1
72	10590.031	-0.006	43.9	56.1	0.1
69	10595.554	-0.006	75.6	24.3	0.1
62	10713.205	-0.006	61.5	38.4	0.1
25	10496.360	-0.011	55.7	44.3	0.0
73	10608.598	0.005	77.4	22.6	0.1
34	10575.252	0.002	83.9	16.0	0.0
87	10294.767	0.004	86.3	13.6	0.1
20	10352.114	0.004	61.3	38.6	0.0
119	10662.753	-0.001	77.3	22.5	0.1
143	10801.142	-0.001	70.9	27.4	1.8
134	10968.075	0.005	80.2	19.5	0.3
49	12053.926	-0.001	82.7	17.3	0.0
71	12511.108	0.009	81.7	18.3	0.0

IV. DEPERTURBATION ANALYSIS

A. Modeling Hamiltonian

The non-adiabatic rovibronic wavefunction $\Psi_j = \sum_i \phi_i \varphi_i$ ($i \in [A^1\Sigma^+, b^3\Pi_{\Omega=0,1,2}]$) corresponding to the j -th rovibronic level of the $A^1\Sigma^+ \sim b^3\Pi$ complex of KCs molecule with the fixed rotational quantum number J and e -symmetry was approximated by the linear combination of the symmetrized electronic-rotational wavefunctions φ_i belonging to a pure Hund's coupling case (**a**) [16]. The expansion coefficients $\phi_i(r)$ are the r -dependent fractional components of

the non-adiabatic vibrational wavefunction $\Phi_j \equiv \|\phi_A, \phi_{b0}, \phi_{b1}, \phi_{b2}\|$ which are determined by the bound solution of the close-coupled (CC) radial equations [21, 22, 25]:

$$\left(-\mathbf{I} \frac{\hbar^2 d^2}{2\mu dr^2} + \mathbf{V}(r; \mu, J) - \mathbf{I} E_j^{CC} \right) \Phi_j(r) = 0 \quad (1)$$

with the conventional boundary $\phi_i(0) = \phi_i(\infty) = 0$ and normalization $\sum_i P_i = 1$ conditions, where $P_i = \langle \phi_i | \phi_i \rangle$ is the fractional partition of the j -th level. Here \mathbf{I} is the identity matrix, E_j^{CC} is the total non-adiabatic energy of rovibronic level of the complex while \mathbf{V} is the symmetric 4×4 matrix of potential energy consists of the diagonal

$$\begin{aligned} V_{1\Sigma^+} &= U_A + B[X + 2] \\ V_{3\Pi_0} &= U_{b0} + B[X + 2] \\ V_{3\Pi_1} &= U_{b1} + B[X + 2] \\ V_{3\Pi_2} &= U_{b2} + B[X - 2] \end{aligned} \quad (2)$$

and non-vanishing off-diagonal

$$\begin{aligned} V_{1\Sigma^+ - 3\Pi_0} &= -\sqrt{2} \xi_{Ab0}^{so} \\ V_{3\Pi_0 - 3\Pi_1} &= -B\sqrt{2X} \\ V_{3\Pi_1 - 3\Pi_2} &= -B\sqrt{2(X-2)} \\ V_{1\Sigma^+ - 3\Pi_1} &= -B\zeta_{Ab1} \sqrt{2X} \end{aligned} \quad (3)$$

matrix elements explicitly depending on reduced mass μ and rotational quantum number J as a parameter:

$$B \equiv \frac{\hbar^2}{2\mu r^2}; \quad X \equiv J(J+1)$$

Hereafter all electronic parameters of the model are assumed to be mass-invariant.

Here $U_A(r)$, $U_{b\Omega}(r)$ are the diabatic PECs of the singlet $A^1\Sigma^+$ and triplet $b^3\Pi_{\Omega=0,1,2}$ sub-states while $\xi_{Ab0}^{so}(r)$ is the relevant spin-orbit coupling matrix element. Besides of strong off-diagonal homogenous $A^1\Sigma^+ \sim b^3\Pi_{\Omega=0}$ interactions the deperturbation model also explicitly consider heterogenous spin-rotational interaction between all $\Omega = 0, 1, 2$ components of the triplet $b^3\Pi$ state [16]. Moreover, the non-equidistant SO splitting functions $A_-^{so} \neq A_+^{so}$ between the $b^3\Pi_{\Omega=0,1,2}$ sub-states

$$U_{b1} = U_{b0} + A_-^{so}; \quad U_{b2} = U_{b1} + A_+^{so} \quad (4)$$

and the indirect coupling $A^1\Sigma^+ \sim b^3\Pi_{\Omega=1}$ parameter ζ_{Ab1} were introduced in the Hamiltonian (2); (3) in order to account implicitly for regular perturbations caused by the remote $^1\Pi$ and $^3\Sigma^+$ states manifold (first of all the $B^1\Pi$ and $c^3\Sigma^+$ states converging to the second dissociation limit, see Fig. 1).

B. Computational details/Fitting procedure

The empirical PECs of the interacting $A^1\Sigma^+$ and $b^3\Pi_0$ states $U_A(r)$, $U_{b0}(r)$ as well as both diagonal $A_{\pm}^{so}(r)$ and the off-diagonal $\xi_{Ab0}^{so}(r)$ spin-orbit functions were represented analytically by the Expanded Morse Oscillator (EMO) function [26]

$$T_e + \mathfrak{D}_e \left[1 - e^{-\alpha(r)(r-r_e)} \right]^2; \quad (5)$$

$$\alpha = \sum_{i=0}^N a_i \left(\frac{r^p - r_{ref}^p}{r^p + r_{ref}^p} \right)^i$$

converging to the appropriate atomic limit. In particular, for all SO functions $T_e^{so} = \xi_{Cs}^{so} - \mathfrak{D}_e^{so}$ where $\xi_{Cs}^{so} \equiv [E_{6^2P_{3/2}} - E_{6^2P_{1/2}}]/3$ is the spin-orbit constant of the Cs atom in the 6^2P state [27, 28]. For diabatic PEC U_A of the singlet state $T_e^A = T_{dis} - \mathfrak{D}_e^A$ while $T_e^{b0} = T_{dis} - \xi_{Cs}^{so} - \mathfrak{D}_e^{b0}$ for the U_{b0} sub-state of the triplet. Here $T_{dis} = \mathfrak{D}_e^X + E_{6^2P} - E_{6^2S}$ is the energy of center of gravity of the $Cs(6^2P)$ doublet (without hfs splitting) [27] referred to the minimum of the ground X -state. The $\mathfrak{D}_e^X = 4069.3 \text{ cm}^{-1}$ value is taken from Ref. [10].

The initial EMO parameters (\mathfrak{D}_e , r_e and a_i) of the relevant PECs were estimated by averaging of the independent *ab initio* results borrowed from Ref's [12, 13, 14] while the required SO functions were constructed using the recent quasi-relativistic estimates of Ref. [14]. Off-diagonal SO function could be empirically determined only in the close vicinity of the crossing point of the diabatic PECs of the interacting $A^1\Sigma^+$ and $b^3\Pi_0$ states. Therefore, the required SO-EMO functions were constrained by fixing of the respective $a_i (i > 0)$ parameters based on the relevant *ab initio* points [14], so only \mathfrak{D}_e^{so} , r_e^{so} and a_0^{so} SO-EMO parameters were rest to be variable in the fit.

The refined parameters of the PECs and SO functions combined with the r -independent $\xi_{Ab1}^{so} = \text{const}$ parameter were determined iteratively during the weighted nonlinear least-squared fitting (NLSF) procedure [16]:

$$\chi_{expt}^2 = \sum_{j=1}^{N_{expt}} \frac{w_j (E_j^{CC} - E_j^{expt})^2}{N_{expt} - M_p}, \quad (6)$$

where $w_j = 1/\sigma_j^2$ is the weight of each level, E_j^{expt} its experimental termvalue and $\sigma_j^{expt} = 0.003-0.01 \text{ cm}^{-1}$ its uncertainty. Here, N_{expt} is the number of experimental termvalues involved while M_p is

the total number of adjusted parameters of the model. Only experimental rovibronic termvalues E_j^{expt} of the most abundant $^{39}\text{K}^{133}\text{Cs}$ isotopomer were included in the fitting procedure. The minimum of the functional (6) was searched by the modified Levenberg-Marquardt algorithm [31] realized by MINPACK software [32].

The analytical mapping procedure based on replacement of the conventional radial coordinate (in Å) by the reduced radial variable $y(r; \bar{r} = 5.2, \beta = 5) = [1 + (\bar{r}/r)^\beta]^{-1}$ was used to transform the initial CC equations (1) into completely equivalent form. Then, the modified CC equations given explicitly in Ref. [33] were solved on the interval $r \in [2.5, 15.5] \text{ Å}$ by the finite-difference (FD) boundary value method [34] with the fixed number of uniform grid points N . The central 5-points FD approximation (FD5) of the kinetic energy term was employed in Eq. (1). The ordinary eigenvalue and eigenfunction problem of the resulting symmetric band matrix was iteratively solved by the implicitly restarted Lanczos method realized in ARPACK software in the shift-inverted spectral transformation mode [35]. The energy error correction for the FD5 method recently invented in the explicit integral form [22] was used to extrapolate to infinite number of grid points the eigenvalue obtained at the fixed number of integration points. The optimized procedure allowed us to attain the absolute accuracy of the calculated energies E_j^{CC} about of 0.001 cm^{-1} using only $N = 1500 - 2000$ grid points.

V. RESULTS AND DISCUSSION

A. Interatomic potentials and spin-orbit functions

The resulting EMO parameters of the deperturbed (diabatic) PECs of the $A^1\Sigma^+$ and $b^3\Pi_0$ states are presented Table II while the respective empirical spin-orbit functions are given in Table III. The parameters reproduce 95% of experimental data field of the $^{39}\text{K}^{133}\text{Cs}$ isotopomer with a standard deviation (SD) of 0.004 cm^{-1} in the framework of the phenomenological model defined by Eq. (2) and Eq. (3). The SD value is well-consistent with the estimated uncertainty of $0.003 - 0.01 \text{ cm}^{-1}$ of the present experiment. The EMO parameters defined by Eq. (5) are given in the EPAPS in double precision format [36]. For convenience the fitted PECs and SO functions

TABLE II: The resulting EMO parameters of the diabatic potential energy curves of the deperturbed $A^1\Sigma^+$ and $b^3\Pi_0$ states. T_{dis} , \mathcal{D}_e and T_e in cm^{-1} , r_{ref} and r_e in \AA , a_i in \AA^{-1} , p is the dimensionless. T_{dis} , r_{ref} and p parameters were fixed in the fit.

Parameter	$A^1\Sigma^+$	$b^3\Pi_0$
T_{dis}	15616.95	
p	3	4
r_{ref}	5.0	4.2
\mathcal{D}_e	5567.546	6599.300
r_e	4.981380	4.179865
a_0	0.44685377	0.56383223
a_1	0.01153475	0.11731134
a_2	0.01224621	0.10163399
a_3	0.12946458	-0.04095288
a_4	0.16407832	-0.37280647
a_5	0.28366171	0.11826773
a_6	-0.27382905	2.22890307
a_7	-0.61363449	0.57576966
a_8	1.05182596	-5.39299688
a_9	0.87045466	-3.16111671
a_{10}	-1.00928649	8.86174318
a_{11}	-0.72414478	4.22763021
a_{12}	0.00055024	-7.36542364
a_{13}		-0.00010791
a_{14}		0.12543766

are represented in the EPAPS by the appropriate point-wise form as well. Furthermore, EPAPS tables contain both experimental and reproduced rovibronic termvalues of the complex as well as their residuals and fractional partitions.

As can be seen from Fig. 7, the singlet A and triplet b state PECs are intersecting in the vicinity of the equilibrium distance r_e of the A -state. As a result, all levels of the singlet state are strongly perturbed and the most significant perturbations take place for low vibrational levels v_A of the A -state. The diabatic (deperturbed) $v_{b0} = 18$ vibrational level of the triplet state is found to be the first one which reach by energy the ground diabatic $v_A = 0$ level of the singlet at low J' -values. However high rotational levels of the $v_A = 0$ basically interact with lower vibrational levels ($v_{b0} < 18$) of the b -triplet since $r_e^b \ll r_e^A$ (see Table IV).

Fig. 7 and 8 demonstrate a good agreement of the derived PECs and SO matrix elements with the *ab initio* quasi-relativistic results [12, 13, 14] both inside and outside the experimental data region $r \in [3.1, 7.8]$ \AA . In particular, Table IV clearly shows that the empirical molecular constants T_e , ω_e and r_e coincide with their *ab initio* counterparts

TABLE III: The resulting EMO parameters of both diagonal A_{\pm}^{so} and off-diagonal ξ_{Ab0}^{so} spin-orbit coupling functions. $\dagger\xi_{Cs}^{so}$, \mathcal{D}_e^{so} and T_e^{so} in cm^{-1} , $\dagger r_{ref}$ and r_e^{so} in \AA , a_i in \AA^{-1} , $\dagger p = 1$ is the dimensionless. \dagger denotes the fixed parameter. The empirical r -independent coupling parameter $\zeta_{Ab1} = 0.04935$.

Parameter	ξ_{Ab0}^{so}	A_-^{so}	A_+^{so}
$\dagger\xi_{Cs}^{so}$		184.68	
$\dagger r_{ref}$	5.3	5.5	
\mathcal{D}_e^{so}	102.998	106.419	101.539
r_e^{so}	5.054338	5.442732	5.576276
a_0	0.31895	0.42157	0.37735
$\dagger a_1$	0.40997	1.02228	
$\dagger a_2$	0.49244	2.23836	
$\dagger a_3$		-1.71726	
$\dagger a_4$		-9.84181	
T_e^{so}	81.68	78.26	83.14

TABLE IV: Comparison of the basic spectroscopic constants available for the KCs $A^1\Sigma^+$ and $b^3\Pi$ states. The T_e and ω_e values are given in cm^{-1} while r_e in \AA . T_e values are referred to the minimum of the X state. The harmonic frequency for the present PECs $U(r)$ is calculated as $\omega_e = \hbar\sqrt{k/\mu}$ [16], where $k = d^2U/dr^2|_{r=r_e}$ is the strength constant.

State	T_e	r_e	ω_e	T_e	r_e	ω_e	T_e	r_e	ω_e
	present			[15]					
$A^1\Sigma^+$	10049	4.98	49.8						
$b^3\Pi_0$	8833	4.18	68.4	8717	4.17	70.3			
$b^3\Pi_1$	8938	4.19	68.3	8856	4.16	71.6			
$b^3\Pi_2$	9044	4.20	68.2	8981	4.15	71.8			
				[12]	[13]	[14]			
$A^1\Sigma^+$	10107	4.93	51.8	9947	4.95	51.8	10203	5.02	48.3
$b^3\Pi_1$	9017	4.16	71.6	8870	4.19	69.9	9049	4.21	68.8

within 1-2%. The arithmetic mean of the empirical diagonal SO matrix elements $(A_-^{so} + A_+^{so})/2$ (see Fig. 8a) agrees with the *ab initio* SO splitting A^{so} from Ref. [14] within few cm^{-1} near a minimum of these functions; (see Eq. (8)). However, the present empirical $A_{\pm}^{so}(r)$ functions evaluated near the equilibrium distance r_e of the triplet b -state are smaller on 20-25 cm^{-1} than their *ab initio* counterparts corresponding to the pure (c) Hund's coupling case [15] (see Table IV). Near the crossing point of singlet and triplet states $r_c \approx 5.1$ \AA (Fig. 7) the empirical off-diagonal SO coupling function ξ_{Ab0}^{so} coincide with *ab initio* result [14] within 1 – 2

cm⁻¹ (Fig. 8b).

The empirical matrix element $B\zeta_{Ab1}$ (see Fig. 9a) reasonably agree with the *ab initio* estimate obtained in the framework of the second order perturbation theory

$$B\zeta_{Ab1} \approx \frac{BL_{A-B}^{\pm}\xi_{B-b}^{so}}{(U_A + U_b)/2 - U_B} \quad (7)$$

by using of the *ab initio* PEC for the $B^1\Pi$ state U_B as well as SO ξ_{B-b}^{so} and angular L_{A-B}^{\pm} coupling matrix elements [14]. Furthermore, the empirical non-equidistant SO splitting of the $b^3\Pi$ -state (Fig. 8 and 9) qualitatively agree with the estimates

$$A_{\pm}^{so} = A^{so} \pm \delta A^{so}; \quad \delta A^{so} \approx \sum_j \frac{|\xi_{b-j}^{so}|^2}{U_b - U_j} \quad (8)$$

where the required PECs U_j for the $j \in a^3\Sigma^+; c^3\Sigma^+; B^1\Pi$ states and relevant SO matrix elements A^{so}, ξ_{b-j}^{so} of the $b^3\Pi$ state were taken from Ref. [14].

B. Details of the $A^1\Sigma^+$ -state interaction with the $b^3\Pi_{\Omega=0,1}$ sub-states

The magnitude of the off-diagonal *homogenous* spin-orbit $A^1\Sigma^+ \sim b^3\Pi_{\Omega=0}$ interaction, see Fig. 8, is comparable with vibrational spacing of the interacting states, see Table IV. This leads to significant regular non-adiabatic shifts of the most experimental level positions of the $A \sim b$ complex with respect to their deperturbed (diabatic) singlet and triplet counterparts. Fig. 10a gives us a typical example of the experimental level positions of the complex given in a reduced scale as function of rotational quantum number J' . As can be seen, the experimental J' -dependence of A state vibrational level identified for small J' as $v_A^* = 1$ (depicted by graph III), is shifted towards higher energies by approximately 75 cm⁻¹, or by about $1.5\omega_e^A$ (compare with diabatic $v_A = 1$). The graphs I - II belong to experimental $v_{b0}^* = 20$ and 21, respectively. The experimental levels are significantly shifted down with respect their dibatic (deperturbed) positions. All three graphs I - III demonstrate a different slope from any of diabatic J' -dependencies. Moreover, the slope is changing with J' demonstrating the singlet-triplet anti-crossing effect which takes place between experimental terms II and III around $J' = 80$ while between I and II around $J' = 130$.

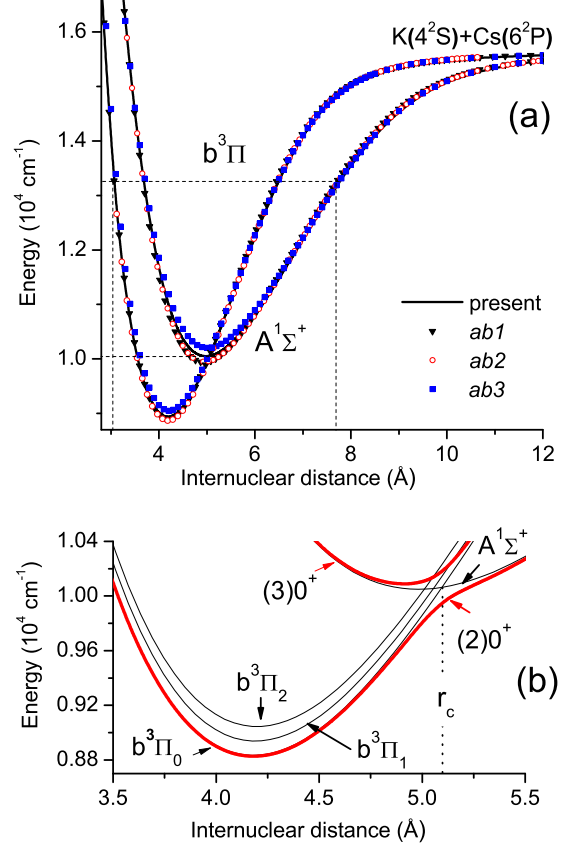


FIG. 7: (Color online) (a) The present empirical (*emp.*) and available *ab initio* (*ab1*-[12]; *ab2*-[13]; *ab3*-[14]) PECs of the $A^1\Sigma^+$ and $b^3\Pi_{\Omega=1}$ states corresponding to the a Hund's coupling case. The insert zooms in the respective PECs around r_e . (b) The present empirical diabatic PECs of the $A^1\Sigma^+, b^3\Pi_{\Omega=0,1,2}$ sub-states and the corresponding adiabatic PECs $(2;3)\Omega=0^+$ in the c coupling case states.

Along with the dominating $A^1\Sigma^+ \sim b^3\Pi_{\Omega=0}$ interaction, weak local *heterogenous* perturbations caused by the $(A-b)_{\Omega=0} \sim b^3\Pi_{\Omega=1}$ indirect interaction are pronounced as sharp irregularities of the order of 1 cm⁻¹ in the vicinity of intersection of experimental term values with diabatic dependencies of the $b^3\Pi_{\Omega=1}$ sub-state. One such example is given by the inset in Fig. 10a while the more detailed analysis of the *heterogenous* perturbation is shown in Fig. 11. The peculiarity of the both cases is connected with experimental observation of two pairs of lines with the same J' -value, namely, for $J' = 113/114$ and $J' = 157/158$ (see Fig. 5b for the second example), giving levels with slightly differ-

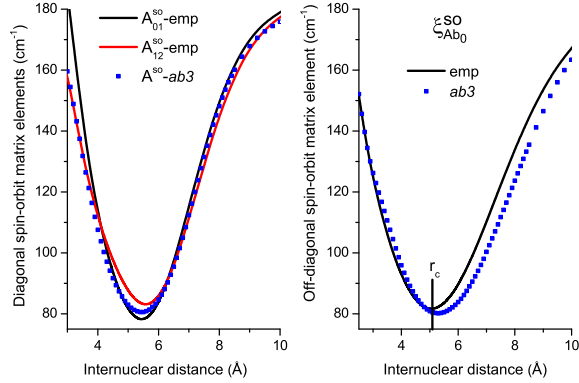


FIG. 8: (Color online) Comparison of the present empirical first order spin-orbit functions with their *ab initio* counterparts (*ab*) from Ref. [14]. (a) the diagonal empirical $A_{\pm}^{so}(r)$ and *ab initio* $A^{so}(r)$ SO splitting functions; (b) the relevant off-diagonal $\xi_{Ab_0}^{so}(r)$ SO coupling functions. r_c is the internuclear distance where diabatic PECs intersect.

ent energies. This is explained by a local perturbation, as a result of which, in each pair of levels with the same J' , see Fig. 11a and the inset in Fig. 10a, one level is predominantly singlet A state, while another one is the triplet $b^3\Pi_{\Omega=1}$ sub-state. It should be noted that at intersection of graphs I and III with diabatic b_1 graph in Fig. 10a only small shifts were observed, without appearance of pairs with the same J' . This typical situation should be attributed to too small fraction of singlet wavefunction in the partner level to observe it.

Both types of interaction are described remarkably well by the present deperturbation model, as is demonstrated by the residuals between the fitted and measured termvalues, see, for example, Fig. 10b and Fig. 11b. Furthermore, the calculated fraction partitions P_i (see Fig. 10c, Fig. 11c, Table I and EPAPS [36]) unambiguously prove a dominant role of the direct SO $A^1\Sigma^+ \sim b^3\Pi_{\Omega=0}$ interaction. Indeed, one can see that smooth variation of the singlet fraction in the total wave function corresponds to the smooth change of the respective termvalues. The sharp resonances at $J' = 113/114$ (Fig. 10c) and $J' = 157/158$ (Fig. 11c) both correspond to the intersection of J' -dependence of the respective experimental termvalues with diabatic dependence for $v_{b_1} = 17$ caused by indirect interaction of A state with the $b^3\Pi_{\Omega=1}$ sub-state. The very small irregularities of partition fractions no-

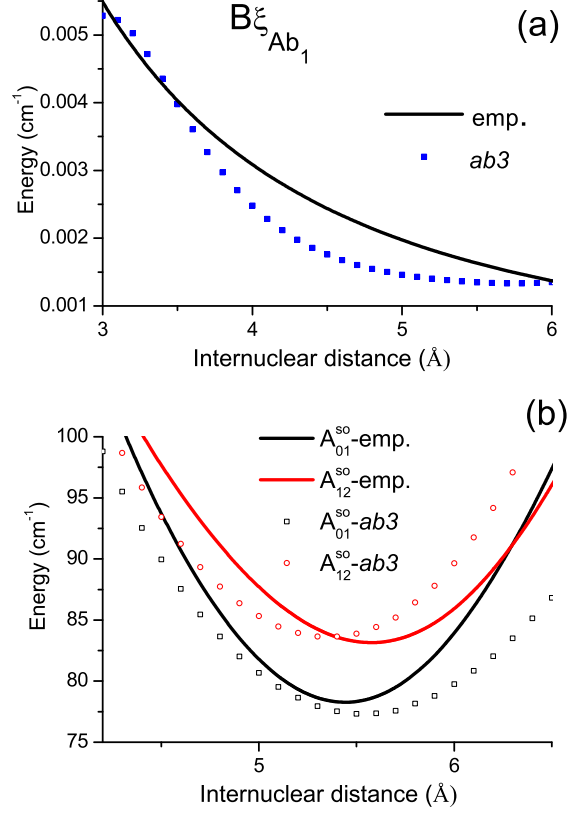


FIG. 9: Comparison of the present empirical and *ab initio* second order spin-orbit functions. (a) the empirical $B\zeta_{Ab_1}$ entering Eq. (3) while *ab initio* function is determined by Eq. (7); (b) the empirical SO splitting functions A_{\pm}^{so} entering Eq. (4) while *ab initio* A_{\pm}^{so} values are calculated by Eq. (8).

ticed on Fig. 10c at $J' = 81$ and 124 indicate the predicted influence of $b^3\Pi_2$ component which has only minor effect on energy and, hence, it could not be observed experimentally.

C. Term values of the $^{41}\text{K}^{133}\text{Cs}$ isotopomer

To confirm mass-invariant properties of the deperturbed parameters the rovibronic termvalues of the $^{41}\text{K}^{133}\text{Cs}$ isotopomer have been predicted and compared with the experimentally observed ones. In the calculation only corresponding reduced mass μ of the isotopomer in the operator kinetic energy Eq. (1) and parameter B in the Eq. (4) of the potential energy matrix defined by Eq. (2) and (3)

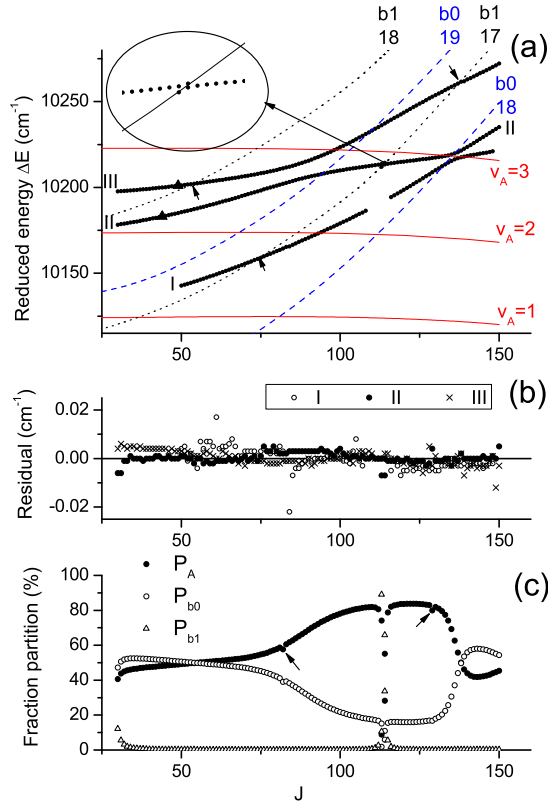


FIG. 10: (a) Fragment of J' -dependence of the experimental term values as well as their deperturbed diabatic singlet and triplet counterparts. Term values are given by the reduced scale: $\Delta E = E - 0.0222 \times J'(J' + 1)$. The graphs I, II, and III denote experimental data. Almost horizontal solid lines refer to diabatic singlet $A^1\Sigma^+$ state in the region $v_A = 1 - 3$; the dashed and dotted lines refer to diabatic triplet sub-states $b^3\Pi_{\Omega=0}$ ($v_{b_0} = 18 - 20$) and $b^3\Pi_{\Omega=1}$ ($v_{b_1} = 17$ and 18), respectively. For small J' the effective vibrational quantum numbers can be attributed as $v_{b_0}^*(\text{I}) = 20$, $v_{b_0}^*(\text{II}) = 21$ and $v_A^*(\text{III}) = 1$. The inset zooms in the splitting caused by the interaction with $v_{b_1} = 17$ term. Arrows mark places of observed weak local perturbations with b_1 sub-state. The triangles mark the levels which give the LIF progressions analyzed in Fig. 13 and 14. (b) Residuals of the fit $E_j^{expt} - E_j^{CC}$ for all respective J' values. (c) Fraction partition of the relevant non-adiabatic wavefunctions P_i for the experimental term values presented by graph II. The sharp resonance at $J' = 113/114$ corresponds to the intersection shown by inset in (a). The arrows in (c) mark the predicted influence of $b^3\Pi_{\Omega=2}$ component.

was substituted. The calculated term values coin-

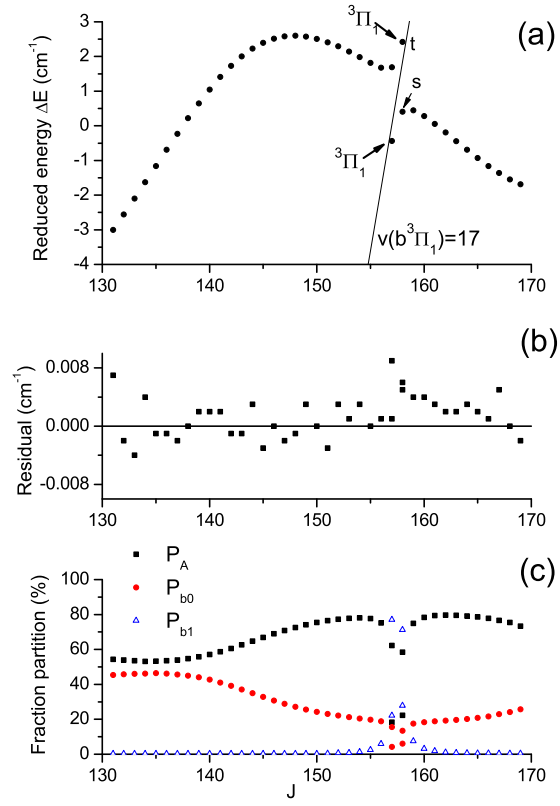


FIG. 11: (Color online) (a) The experimental term values around the local $J' = 157/158$ perturbation (see Fig. 5b) caused by the $v_{b_1} = 17$ level of the diabatic $b^3\Pi_{\Omega=1}$ sub-state (marked by the solid line). Term values are presented by the reduced scale: $\Delta E = E - 10266 - 0.0237J'(J' + 1)$. (b) Residuals of the fit $E^{expt} - E^{CC}$ for respective J' values. (c) The respective partition functions P_i .

cide with the experimental data (see Table I) with standard deviation of 0.0055 cm^{-1} . In absence of any adjustment of the parameters, the agreement even for the highly excited and strongly mixing levels can be assumed as excellent.

D. Intensity distribution in the $A^1\Sigma^+ \sim b^3\Pi \rightarrow X^1\Sigma^+$ LIF progressions

As well-known a nodal structure of non-adiabatic vibrational wavefunctions is rather sensitive to strong intramolecular perturbations [16, 21, 22]. Therefore, a comparison of the experimental relative intensity distributions in a band

structure $A \sim b \rightarrow X(v_X)$ LIF progressions with their theoretical counterparts would be a critical independent test on a completeness of the above energy-based deperturbation analysis.

The theoretical transition probabilities $I_{A \sim b \rightarrow X}$ were estimated as:

$$\begin{aligned} I_{A \sim b \rightarrow X}(v_X) &\sim \nu_{A \sim b \rightarrow X}^4 M_{A \sim b \rightarrow X}^2 \quad (9) \\ \nu_{A \sim b \rightarrow X} &= E^{CC}(J') - E_X(v_X; J_X = J' \pm 1) \\ M_{A \sim b \rightarrow X} &= \langle \phi_A | d_{AX} | v_X \rangle \end{aligned}$$

where $d_{AX}(r)$ is the *ab initio* $A - X$ transition dipole moment from Ref's [13, 14]. The power of 4 used in the transition wavenumber $\nu_{A \sim b \rightarrow X}$ assumes that the detector is proportional to the intensity of the incoming fluorescence light. The rovibronic energies E_X and eigenfunctions $|v_X\rangle$ of the ground $X^1\Sigma^+$ state were obtained by solving the single channel radial equation with the empirical PEC from Ref. [10]. Hereafter, both experimental and calculated intensities obtained for P and R -branches separately were then averaged since they basically were very close to each other.

The remarkable agreement observed (see Fig. 12a) between the simulated and experimental intensity distribution in the very long $v_X \in [0, 80]$ LIF progression originating from the high rovibronic level of the complex convincingly proves a high reliability of the deperturbation model used. It is easily seen from Fig. 12b that the non-adiabatic wavefunction $\phi_A(r)$ of the singlet A -state, which is responsible for the complicated oscillation behavior of intensity observed on Fig. 12a, is only weakly perturbed by the triplet b -state. The respective fraction of the singlet state P_A is dominating here being 0.81.

To elucidate influence of the strong off diagonal homogenous SO $A^1\Sigma^+ \sim b^3\Pi_{\Omega=0}$ interactions on a nodal structure of the perturbed wavefunctions we have measured and simulated respective intensity distributions in $A \sim b \rightarrow X(v_X)$ LIF progressions originating from two rovibronic levels (marked by solid triangles on Fig. 10a) which are close to each other by J' and term values. These levels have, however, a quite different admixture of the $b^3\Pi_0$ component. The agreement between calculated and experimental intensities is found to be, once more, remarkably good (see Fig. 13a,b). For both levels the $I(v_X)$ functions (Fig. 13a,b) obey very well to so-called ‘‘Condon reflection approximation’’ [16] since the v_X dependence of $I(v_X)$ mimic the r -dependence of the initial wavefunction of the complex, $|\phi_A(r)|^2$; see Fig. 13c. Indeed, in according to three lobes of non-adiabatic wavefunctions

$\phi_A(r)$ of singlet fraction depicted on Fig. 13c the respective intensity distributions show three pronounced maximums which are clearly seen on Fig. 13a,b. At the same time, due to the strong homogenous interaction an amplitude of the lobes of two wavefunctions are well distinguished leading to quiet different intensity distribution functions (compare Fig. 13a with Fig. 13b). It is interesting that the most dramatic changes in a shape of non-adiabatic wavefunctions are observed near the crossing point r_c of the interacting states (Fig. 7b). For instance, the $\phi_A(r)$ of the $J' = 44$ level has very small additional lobe near $r \approx 5.2$ Å. This lobe provides small but not negligible peak located at $v_X = 16$ on the intensity distribution function; see Fig. 13b.

It also should be noticed that in according to ‘‘oscillation theorem’’ [37] the $J' = 49$ level mentioned above would be assigned to the $v_A = 2$ vibrational state since its wavefunction $\phi_A(r)$ has two nodes at least. However, from the energy viewpoints (Fig. 10a) and P_A analysis it can be assigned as $v_A^* = 1$. The detailed analysis of this effect (conventional *oscillation* theorem breakdown caused by strong homogeneous perturbations) has been done separately in our accompanied paper [39].

To investigate the influence of the local *heterogeneous* ($A - b$) $_{\Omega=0} \sim b^3\Pi_{\Omega=1}$ interaction on a nodal structure of wavefunctions we have measured and simulated intensity distributions in the LIF progressions originating from two mutually perturbed levels, shown on Fig. 11a, with the same $J' = 158$ values. The agreement between calculated and experimental values, once more, is remarkably good (Fig. 14a,b). It is surprising to see that the intensity distributions for both levels are found to be almost identical; the one level (marked as ‘‘s’’) having the lower energy demonstrates a dominant singlet $A^1\Sigma^+$ character while the higher-lying level (marked as ‘‘t’’) has significant $b^3\Pi_{\Omega=1}$ component. The calculation of the respective non-adiabatic wavefunctions $\phi_A^{s/t}(r)$ (see Fig. 14c) confirms that their nodal structure is coinciding while the amplitudes are different. Indeed, the wavefunctions relates to each other as

$$\sqrt{P_A^t} \phi_A^s(r) = \sqrt{P_A^s} \phi_A^t(r). \quad (10)$$

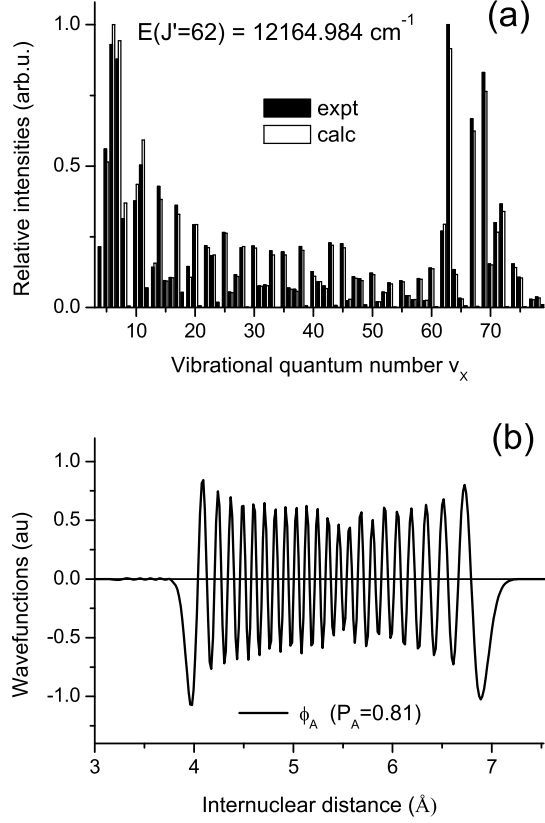


FIG. 12: (a) The experimental and calculated intensity distribution in the long LIF progression (see Fig. 2) originating from the high rovibronic level $E_{A\sim b}(J' = 62)$ of the $A \sim b$ complex. (b) Respective fraction of the non-adiabatic $\phi_A(r)$ wavefunction of the A -state ($P_A = \langle \phi_A | \phi_A \rangle = 0.81$).

E. Simulation of the optical cycle

$a^3\Sigma^+ \rightarrow A^1\Sigma^+ \sim b^3\Pi \rightarrow X^1\Sigma^+$

Since the predictive abilities of the derived de-perturbation parameters of the $A \sim b$ complex were unambiguously proved above we have used them to simulate a wavenumbers

$$\begin{aligned} \nu_{a \rightarrow A\sim b}^{PUMP} &= E_j^{CC}(J' = 1) - E_a(N_a = 0) \\ \nu_{A\sim b \rightarrow X}^{DUMP} &= E_j^{CC}(J' = 1) - E_X(v_X = 0; J_X = 0) \end{aligned}$$

and transition moments

$$\begin{aligned} M_{A\sim b \rightarrow a}^{PUMP} &= |\langle \phi_{b\Omega} | d_{ba} | \chi_a \rangle| \\ M_{A\sim b \rightarrow X}^{DUMP} &= |\langle \phi_A | d_{AX} | \chi_X \rangle| \end{aligned}$$

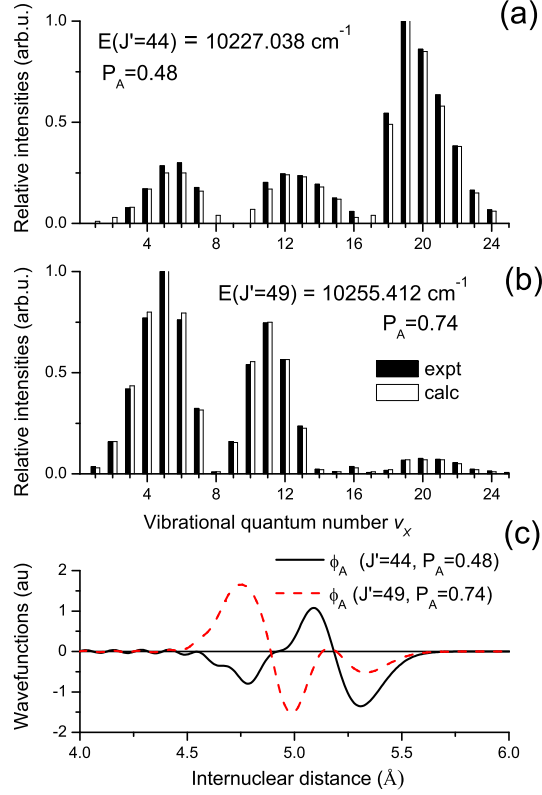


FIG. 13: The experimental and calculated intensity distributions in LIF progressions originating from close-lying rovibronic levels of the $A \sim b$ complex (marked by the solid triangles in Fig. 10): (a) for the $v_{b0}^* = 21; J' = 44$ having an admixture of the triplet $b^3\Pi_{\Omega=0}$ component ($P_{b0} = \langle \phi_{b0} | \phi_{b0} \rangle = 0.52$); (b) for the $v_A^* = 1; J' = 49$ level having a dominant singlet $A^1\Sigma^+$ character ($P_A = 0.74$). (c) Respective non-adiabatic wavefunctions $\phi_A(r)$ of the singlet A -state.

for the PUMP-DUMP optical cycle $a^3\Sigma^+ \rightarrow A^1\Sigma^+ \sim b^3\Pi \rightarrow X^1\Sigma^+$ which has been proposed in Ref. [5] to transform an ultracold $K(3^2S) + Cs(6^2S)$ colliding pairs in their absolute ground state. The excitation $a \rightarrow A \sim b$ and emission $A \sim b \rightarrow X$ transitions presented in Table V correspond to the most pronounced transition probabilities of the two-steps conversion process. Table V also contains the predicted radiative lifetimes $\tau_{A\sim b}$ [38]

$$\frac{1}{\tau_{A\sim b}} = \frac{8\pi^2}{3\hbar c} \times \left[\langle \phi_A | \Delta U_{AX}^3 d_{AX}^2 | \phi_A \rangle + \langle \phi_b | \Delta U_{ba}^3 d_{ba}^2 | \phi_b \rangle \right] \quad (11)$$

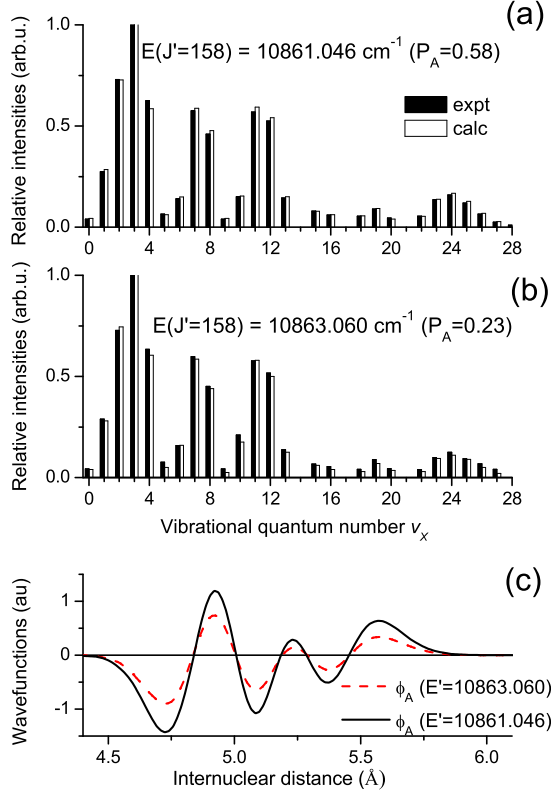


FIG. 14: The experimental and calculated intensity distributions in the LIF progressions originating from two mutually perturbed levels of the $A \sim b$ complex with the same $J' = 158$ -value (see Fig. 11a): (a) having dominant singlet $A^1\Sigma^+$ character ($P_A^s = 0.58$; $P_{b0}^s = 0.14$; $P_{b1}^s = 0.28$), marked in Fig. 11a by “s”; (b) having dominant $b^3\Pi_{\Omega=1}$ component ($P_A^t = 0.23$; $P_{b0}^t = 0.06$; $P_{b1}^t = 0.71$), marked by “t” in Fig. 11a. (c) Respective non-adiabatic $\phi_A^{s/t}(r)$ wavefunctions of the A -state.

and branching ratios of the spontaneous emission $R_{A\sim b}$

$$R_{A\sim b} = \frac{8\pi^2}{3\hbar c} \nu_{A\sim b-X}^3 M_{A\sim b-X}^2 \tau_{A\sim b} \quad (12)$$

from the intermediate level of the complex with $J' = 1$ to the absolute ground level. Here, $\Delta U_{ij} = U_i - U_j$ is the difference potential. Both $\tau_{A\sim b}$ and $R_{A\sim b}$ values are also useful for estimating the efficiency of the simple PUMP-spontaneous emission process for producing population in the absolute ground level.

The probabilities of PUMP transition were estimated using the *ab initio* dipole transition mo-

TABLE V: The wavenumbers $\nu_{a\rightarrow A\sim b}^{PUMP}$, $\nu_{A\sim b\rightarrow X}^{DUMP}$ (in cm^{-1}) and transition moments $M_{A\sim b-X}^{DUMP}$, $M_{A\sim b-a}^{DUMP}$ (in *a.u.*) predicted for the most favorable stimulated Raman process $a^3\Sigma^+(N_a = 0) \rightarrow A^1\Sigma^+ \sim b^3\Pi(J' = 1) \rightarrow X^1\Sigma^+(v_X = 0; J_X = 0)$. The $\nu_{a\rightarrow A\sim b}^{PUMP}$ values are given with respect to the common dissociation energy of the ground singlet X and triplet a states (see Fig.1). The $\tau_{A\sim b}$ (in *ns*) and $R_{A\sim b}$ (in %) are the radiative lifetimes and branching ratios of the spontaneous emission, respectively.

$\nu_{a\rightarrow A\sim b}^{PUMP}$	$\nu_{A\sim b\rightarrow X}^{DUMP}$	$M_{A\sim b-a}^{PUMP}$	$M_{A\sim b-X}^{DUMP}$	$\tau_{A\sim b}$	$R_{A\sim b}$
7375.17	11410.643	1.03(-2)	0.189	61	1
7311.92	11347.386	5.89(-3)	0.223	83	1
7182.31	11217.785	4.06(-3)	0.499	40	3
7121.44	11156.906	7.48(-3)	0.453	69	4
7100.85	11136.325	5.74(-3)	0.528	40	3
7047.54	11083.010	7.77(-3)	0.795	35	6
7018.76	11054.231	6.02(-3)	0.326	73	2
6990.99	11026.460	5.08(-3)	0.674	52	6
6967.69	11003.164	6.66(-3)	0.818	44	8
6910.53	10946.001	3.66(-3)	1.117	34	11
6834.33	10869.801	1.54(-3)	1.086	53	16
6811.20	10846.672	2.56(-3)	0.486	62	4
6771.69	10807.165	3.45(-3)	1.352	34	16
6764.03	10799.497	6.12(-3)	0.375	117	4
6700.45	10735.916	9.81(-3)	1.224	59	22
6630.94	10666.413	7.46(-3)	1.408	35	17
6590.33	10625.805	3.72(-3)	0.512	59	4
6564.47	10599.938	7.16(-3)	1.092	54	15
6544.13	10579.603	3.40(-3)	0.789	46	7
6488.40	10523.869	2.45(-3)	1.104	34	10
6343.98	10379.452	5.38(-3)	0.613	34	3
6268.13	10303.598	8.10(-3)	0.338	43	1

ment $d_{ba}(r)$ from Ref. [14] and adiabatic wavefunction $|v_a\rangle$ of the initial $a^3\Sigma^+$ state [11] calculated for a virtual vibrational level with the zero bounding energy $E_a(N = 0) = 0$. The singlet-triplet $X^1\Sigma^+ \sim a^3\Sigma^+$ perturbation of the initial level caused by a hyperfine Fermi contact interaction [11] was neglected. The upper limit of the termvalues for the $A \sim b$ complex $E_j^{CC}(J' = 1)$ was limited by 13200 cm^{-1} in order to avoid an extrapolation error outside the experimental region. The wavenumbers and transition probabilities for arbitrary rovibronic levels of the $A \sim b$ complex and ground singlet X and triplet a states can be generated by a request.

VI. CONCLUSIONS

We have accomplished both experimental and deperturbation studies of the fully mixed $A^1\Sigma^+$ and $b^3\Pi$ states of the KCs molecule based on a direct reduction of highly accurate Fourier-transform spectroscopy data on rovibronic termvalues of the $A \sim b$ complex to potential energy curves and spin-orbit coupling functions for the mutually perturbed states.

The experimental data field starts from the lowest vibrational level $v_A^* = 0$ of the singlet and nonuniformly covers rotational quantum numbers $J \in [7, 225]$ in the energy range $E^J \in [10040, 13250] \text{ cm}^{-1}$. Overall 42 adjusted fitting parameters have been required to reproduce more than 3400 rovibronic termvalues of the $A \sim b$ complex with a standard deviation of 0.004 cm^{-1} which is absolutely consistent with the uncertainty of the experiment of $0.003\text{-}0.01 \text{ cm}^{-1}$. Reliability of the derived structure parameters was unambiguously confirmed by a good agreement of the predicted termvalues of $^{41}\text{K}^{133}\text{Cs}$ isotopomer and relative intensity distributions in the $A \sim b \rightarrow X(v_X)$ LIF progressions with their experimental counterparts.

Besides of the dominating *homogeneous* spin-orbit $A^1\Sigma^+ \sim b^3\Pi_{\Omega=0}$ interactions the local *heterogeneous* $A^1\Sigma^+ \sim b^3\Pi_{\Omega=1}$ perturbations have been discovered in the LIF spectra and their impact on a nodal structure of the non-adiabatic vibrational wavefunctions of the complex have been analyzed by means of specially measured intensity distributions. It was found that the *homogeneous* perturbations can change dramatically a shape of wavefunctions (including even total numbers and position of their nodes) whereas the *heterogeneous* perturbations affect only on amplitude of the wavefunction in according to its fraction partition.

The systematic deviations greater then 0.01 cm^{-1} of the experimental and reproduced termvalues are still observed mostly for lying higher then 12000 cm^{-1} rovibronic levels of the complex es-

pecially when they poses the significant admixture of the $b^3\Pi_{\Omega=1}$ component. This drawback of the deperturbation model could be attributed to the neglected influence of first order spin-orbit and electronic-rotational interactions of the $A \sim b$ complex with nearest $c^3\Sigma^+$ state (Fig. 1).

The strong $A^1\Sigma^+ \sim b^3\Pi$ spin-orbit interaction opens a window for direct observation of the formally spin-forbidden and basically very weak $b^3\Pi - X^1\Sigma^+$ transitions originating from the rovibronic levels of the b -state lying below $v_A = 0$ of the perturbing $A^1\Sigma^+$ state. This work is in a progress.

The Table V shows that the efficiency of the proposed conversion cycle $a^3\Sigma^+(N=0) \rightarrow A^1\Sigma^+ \sim b^3\Pi(J'=1) \rightarrow X^1\Sigma^+(v_X=0; J_X=0)$ is limited by its absorption part which requires a rather high power laser source generating in not very favorable spectral diapason. This limitation caused by a very weak $b - a$ triplet transition dipole moment $d_{ba}(r)$ in the considered r -range [13, 14], has been discovered in the analogue cycle of NaRb [21] and NaCs [22] molecules. Nevertheless, relative high efficiency of the single step PUMP- spontaneous emission transitions observed for the particular levels of the $A \sim b$ complex is encouraging for planning such experiments in the future.

Acknowledgments

The authors are indebted to A. Pashov for providing the program package for identification and analysis of LIF progressions. We are grateful to Dr. Andrei Jarmola for providing the laser diodes built in home made external cavity resonators and to V. Zuters for his help in spectra analysis. The support from the Latvian Science Council grant Nr 09.1036 is gratefully acknowledged by Riga team. Moscow team thanks for the support of Federal Program "Scientists and educators for innovative Russia 2009-2013", contract P 2280.

[1] J.M.Hutson and P.Soldan, International Reviews in Physical Chemistry, **25**, No. 4, 497526 (2006).
 [2] H. P. Büchler, E. Demler, M. Lukin, A. Micheli, Phys. Rev. Lett. **98**, 060404 (2007).
 [3] D. DeMille, Phys. Rev. Lett. **88**, 067901 (2006).
 [4] T. V. Tscherebul and R. V. Krems, Phys. Rev. Lett. **97**, 083201 (2006).
 [5] W. C. Stwalley, Eur. Phys. J. D **31**, 221 (2004).
 [6] S. Ghosal, R. J. Doyle, C. P. Koch, and J. M. Hut-

son, New Journal of Physics **11**, 055011 (2009).
 [7] J. M. Sage, S. Sainis, T. Bergeman, and D. DeMille, Phys. Rev. Lett. **94**, 203001 (2005).
 [8] A. J. Kerman, J. M. Sage, S. Sainis, T. Bergeman, and D. DeMille, Phys. Rev. Lett. **92**, 153001 (2004).
 [9] K. Pilch, A. D. Lange, A. Prantner, G. Kerner, F. Ferlaino, H.-C. Nägerl, and R. Grimm, Phys. Rev. A **79**, 042718 (2009).

- [10] R. Ferber, I. Klincare, O. Nikolayeva, M. Tamanis, H. Knöckel, E. Tiemann, and A. Pashov, *J. Chem. Phys.* **128**, 244316 (2008).
- [11] R. Ferber, I. Klincare, O. Nikolayeva, M. Tamanis, H. Knöckel, E. Tiemann, and A. Pashov, *Phys. Rev. A* **80**, ??? (2009).
- [12] M. Korek, A.R. Allouche, K. Fakhreddine, and A. Chaalan, *Can. J. Phys.* **78**, 977 (2000).
- [13] M. Aymar and O. Dulieu, personal communications (2008).
- [14] J.T. Kim, Y. Lee and A.V. Stolyarov, *J. Mol.Spectroscopy*, **256**, 5767 (2009).
- [15] M. Korek, Y. A. Moghrabi, and A. R. Allouche, *J. Chem. Phys.* **124**, 094309 (2006).
- [16] H. Lefebvre-Brion and R.W. Field, *The Spectra and Dynamics of Diatomic Molecules*, (Academic Press, New York, 2004).
- [17] C. Amiot, O. Dulieu, and J. Verges, *Phys. Rev. Lett.* **83**, 2316 (1999).
- [18] H. Salami, T. Bergeman, B. Beser, J. Bai, A. M. Lyyra, J. Huennekens, S. Kotochigova, C. Lisdat, A. Stolyarov, O. Dulieu, P. Crozet and A. J. Ross, *Phys. Rev. A* **80**, 022515 (2009).
- [19] M. Tamanis, R. Ferber, A. Zaitsevskii, E. A. Pazyuk, A. V. Stolyarov, H. Chen, J. Qi, H. Wang, and W. C. Stwalley, *J. Chem. Phys.*, **117**, 7980 (2002).
- [20] T. Bergeman, C.E. Fellows, R.F. Gutterres, and C. Amiot, *Phys. Rev. A* **67**, 050501 (R), (2003).
- [21] O. Docenko, M. Tamanis, R. Ferber, E.A. Pazyuk, A. Zaitsevskii, A.V. Stolyarov, A. Pashov, H. Knöckel, and E. Tiemann, *Phys. Rev. A* **75**, 042503 (2007).
- [22] J. Zaharova, M. Tamanis, R. Ferber, A. N. Drozdova, E. A. Pazyuk, and A. V. Stolyarov, *Phys. Rev. A* **79**, 012508 (2009).
- [23] O. Docenko, M. Tamanis, R. Ferber, T. Bergeman, S. Kotochigova, A. V. Stolyarov, Andreia de Faria Nogueira and C. E. Fellows, *Phys. Rev. A.*, to be submitted (2009).
- [24] D. DeMille, S. Sainis, J. Sage, T. Bergeman, S. Kotochigova, and E. Tiesinga, *Phys. Rev. Lett* **100**, 043202 (2008).
- [25] V.V.Meshkov, A.Zaitsevskii, E.A.Pazyuk, A.V.Stolyarov, R.Bruhl and D.Zimmermann, *J.Chem.Phys.*, **123**, 204307 (2005).
- [26] E.G.Lee, J.Y.Seto, T.Hirao, P.F.Bernath and R.J.LeRoy, *J.Mol.Spectrosc.* **194**, 197 (1999).
- [27] K.B.S.Eriksson and I.Wenaker, *Phys.Scr.* **1**, 21 (1970).
- [28] K.-H.Weber and C.J.Sansonetti, *Phys.Rev.A* **35**, 4650 (1987).
- [29] R.J. Le Roy : A computer program to fit pointwise potentials to selected analytic functions. <http://leroy.uwaterloo.ca/programs> University of Waterloo Chemical Physics Research Report CP-663R. 2007.
- [30] I.Dabrowski, D.W.Tokaryk, and J.K.G.Watson, *J.Mol.Spectrosc.* **189**, 95 (1998).
- [31] W. H. Press, S. A. Teukolsky, W. T. Vetterling, and B. P. Flannery, *Numerical Recipes in Fortran 77* (Cambridge University Press, 1999).
- [32] J.More, B.Garbow, and K.Hillstrom, MINPACK software for solving nonlinear equations and nonlinear least squares problems. <http://www.netlib.org/minpack>, University of Chicago, Argonne National Laboratory (1999).
- [33] V.V.Meshkov, A.V.Stolyarov and R.J.Le Roy, *Phys. Rev. A*, **78**, 052510 (2008).
- [34] D.G.Truhlar, *J.Comp.Phys.* **10**, 123 (1972).
- [35] R. B. Lenoucq, D. C. Sorensen, and C. Yang, ARPACK User's Guide: *Solution of Large Scale Eigenvalue Problems with Implicitly Restarted Arnoldi Methods* (1997); <http://www.netlib.org/arpack>.
- [36] EPAPS archive.
- [37] L.D. Landau and E.M. Lifshitz, *Quantum Mechanics*, (Pergamon, New York, 1965).
- [38] T. Kiyoshima, S. Sato, E.A. Pazyuk, A.V. Stolyarov, M.S. Child, *J.Chem.Phys.*, **118**, 121 (2003).
- [39] V.I. Pupyshev, E.A. Pazyuk, A.V. Stolyarov, M. Tamanis, R. Ferber, *Phys. Chem. Chem. Phys.*, submitted (2009).